

OPEN

# Integration of amorphous ferromagnetic oxides with multiferroic materials for room temperature magnetoelectric spintronics

Humaira Taz<sup>1,2,11</sup>, Bhagwati Prasad<sup>1,11\*</sup>, Yen-Lin Huang<sup>1</sup>, Zuhuang Chen<sup>1,3</sup>, Shang-Lin Hsu<sup>1</sup>, Ruijuan Xu<sup>1</sup>, Vishal Thakare<sup>1</sup>, Tamil Selvan Sakthivel<sup>4</sup>, Chenze Liu<sup>5</sup>, Mark Hettick<sup>6</sup>, Rupam Mukherjee<sup>7</sup>, Sudipta Seal<sup>8</sup>, Lane W. Martin<sup>1,9</sup>, Ali Javey<sup>6</sup>, Gerd Duscher<sup>5</sup>, Ramamoorthy Ramesh<sup>1\*</sup> & Ramki Kalyanaraman<sup>2,10\*</sup>

A room temperature amorphous ferromagnetic oxide semiconductor can substantially reduce the cost and complexity associated with utilizing crystalline materials for spintronic devices. We report a new material ( $\text{Fe}_{0.66}\text{Dy}_{0.24}\text{Tb}_{0.1}\text{O}_{7-x}$  (FDTO), which shows semiconducting behavior with reasonable electrical conductivity ( $\sim 500$  mOhm-cm), an optical band-gap (2.4 eV), and a large enough magnetic moment ( $\sim 200$  emu/cc), all of which can be tuned by varying the oxygen content during deposition. Magnetoelectric devices were made by integrating ultrathin FDTO with multiferroic  $\text{BiFeO}_3$ . A strong enhancement in the magnetic coercive field of FDTO grown on  $\text{BiFeO}_3$  validated a large exchange coupling between them. Additionally, FDTO served as an excellent top electrode for ferroelectric switching in  $\text{BiFeO}_3$  with no sign of degradation after  $\sim 10^{10}$  switching cycles. RT magneto-electric coupling was demonstrated by modulating the resistance states of spin-valve structures using electric fields.

Spintronics aims to utilize the charge and spin of electrons in order to revolutionize technologies for information storage and logic by bringing them together onto a single chip<sup>1,2</sup>. Current state-of-the-art in magnetoelectronics is based on using multilayers of crystalline oxides in which significant effort must be placed in achieving low defect densities through careful materials selection and processing routes<sup>3-8</sup>. Thin film amorphous semiconductors are excellent candidates for spintronic applications related to switching, storage, and logic for multiple reasons<sup>9-20</sup>. Amorphous films have the advantage that they can be deposited at room temperature, making it possible to integrate them for electronic applications with a wider spectrum of material types.

The ternary amorphous oxide system of In-Ga-Zn-O has been successfully utilized to fabricate transparent channel layers in thin film transistors for display applications<sup>17,21-23</sup>. These materials exhibit a suitable combination of transparency, conductivity, mobility, and carrier concentration - all properties needed for switching applications - but they do not possess room-temperature magnetism. Therefore, while control of electronic transport

<sup>1</sup>Department of Materials Science and Engineering, University of California, Berkeley, CA, 94720, USA. <sup>2</sup>Bredesen Center, University of Tennessee, Knoxville, TN, 37996, USA. <sup>3</sup>School of Materials Science and Engineering, Harbin Institute of Technology, Shenzhen, 518055, P. R. China. <sup>4</sup>Advanced Materials Processing and Analysis Center (AMPAC), Materials Science and Engineering (MSE) Department, University of Central Florida, Orlando, FL, 32816, USA. <sup>5</sup>Department of Materials Science and Engineering, University of Tennessee, Knoxville, TN, 37996, USA. <sup>6</sup>Department of Electrical Engineering and Computer Sciences, University of California, Berkeley, California, 94720, USA. <sup>7</sup>Department of Physics, Lovely Professional University, Phagwara, Punjab, 144411, India. <sup>8</sup>College of Medicine, University of Central Florida, Orlando, FL, 32827, USA. <sup>9</sup>Materials Sciences Division, Lawrence Berkeley National Laboratory, Berkeley, California, 94720, USA. <sup>10</sup>Department of Chemical and Biomolecular Engineering, University of Tennessee, Knoxville, TN, 37996, USA. <sup>11</sup>These authors contributed equally: Humaira Taz and Bhagwati Prasad. \*email: [bprasaditk@gmail.com](mailto:bprasaditk@gmail.com); [rramesh@berkeley.edu](mailto:rramesh@berkeley.edu); [ramki@utk.edu](mailto:ramki@utk.edu)

is on a relatively good footing, the use of amorphous semiconductors for magnetoelectric spintronics has not yet emerged. Several groups have attempted to introduce magnetism into semiconductors by doping<sup>24</sup>. For instance, conventional III-V semiconductors such as GaAs have been doped with magnetic cations to form dilute magnetic semiconductors. However, these materials have still not achieved room temperature ferromagnetism. On the other hand, dilute magnetic oxides have been prepared by doping transparent heavy transition-metal oxides with magnetic cations<sup>25–27</sup> and these have shown to have Curie temperatures above 300 K. A few complex oxides, such as  $\text{La}_{0.7}\text{Sr}_{0.3}\text{MnO}_3$ <sup>28</sup>,  $\text{Sr}_2\text{FeMoO}_6$ <sup>29</sup>, and  $\text{Fe}_3\text{O}_4$ <sup>30,31</sup> display room-temperature magnetism and metallic conductivity. However, all of these magnetic systems require good crystallinity in order to preserve the room temperature magnetism and metallicity that arises from long range spin order; they lose their magnetic order when disordered or highly defective.

Magnetoelectric multiferroics provide a pathway to control the magnetic state of such devices with an applied electric field for low-power operation<sup>2</sup>. Recent studies have demonstrated the use of spin valves made out of conventional ferromagnets such as Co-Fe to demonstrate magnetoelectric coupling<sup>32</sup>. However, one concern with such an approach is the formation of strong Schottky barriers at the interface between the metal and the oxide ferroelectric; this invariably leads to degradation issues such as polarization fatigue<sup>33–35</sup>, imprint and in the case of ferromagnets such as CoFe, the possibility for interfacial oxidation of the Co<sup>36</sup>. In contrast, oxide metals such as La-Sr-Co-O<sub>3</sub>, SrRuO<sub>3</sub> have been demonstrated to show a strong resistance to such interfacial degradation, mainly because they form Ohmic (or almost Ohmic) contacts to the ferroelectrics<sup>33–35</sup>. Furthermore, such oxide metals are able to accommodate the transport of charged oxygen vacancies and thus prevent the formation of interfacial charged layers that have been identified as a possible cause for the degradation. On the other hand, ferromagnetic oxides, such as  $\text{La}_{0.7}\text{Sr}_{0.3}\text{MnO}_3$  and  $\text{Fe}_3\text{O}_4$ , have been integrated with  $\text{BiFeO}_3$  for magnetoelectric switching applications but exhibit coupling only at low temperature (<100 K)<sup>36</sup>. Thus, there is a need for a ferromagnetic oxide that has reasonable conductivity and large enough magnetic moment at room temperature (i.e., that can be sensed from the outside environment without the need for sophisticated sensing apparatus) and is able to withstand the deleterious effects of transport of charged point defects. We note that in this regard, while a large number of crystalline oxide metals have been explored, amorphous oxides have not been that well studied. Recent reports have emerged of amorphous materials made from iron and lanthanide systems that appear to show promising electronic or magnetic behavior<sup>37,38</sup> and this forms the background for our studies.

In this work, we report the synthesis, characterization, and magnetoelectric manifestation of an amorphous semiconducting and ferromagnetic oxide thin-film material grown by pulsed-laser deposition (PLD) from the Terfenol-D ( $\text{Fe}_{1.92}\text{Dy}_{0.7}\text{Tb}_{0.3}$ ) metallic system under varying oxygen background pressures ranging from  $10^{-7}$  to  $10^{-3}$  Torr. The films were deposited at room temperature onto fused quartz substrates or single crystalline  $\text{BiFeO}_3/\text{SrRuO}_3/\text{SrTiO}_3(001)$  substrates using PLD (for details, see Methods section). Microscopic evidence for a homogeneous amorphous microstructure was obtained using high-resolution transmission electron microscopy (TEM), while the chemical composition and oxidation state of the  $(\text{Fe}_{0.66}\text{Dy}_{0.24}\text{Tb}_{0.1})_3\text{O}_{7-x}$  films was determined using electron energy loss spectroscopy (EELS) and X-ray photoelectron spectroscopy (XPS). Electrical conduction in the films occurs by variable range hopping with conductivity decreasing with increasing oxygen pressure. Room-temperature magnetic measurements using a SQUID magnetometer revealed ferromagnetic hysteresis with a magnetic moment and coercivity decreasing and increasing, respectively, with increasing oxygen pressure. X-ray magnetic circular dichroism (XMCD) identified the source of magnetism to be the  $\text{Fe}^{2+}/\text{Fe}^{3+}$  cations with the total moment of the system being highly dependent on the ratio of the two valence states of iron. The pressure-dependent measurements revealed that films deposited with oxygen pressure in the range of  $1-3 \times 10^{-6}$  Torr had a promising combination of properties for spintronic applications, including a high magnetic moment (~400 emu/cc) and low resistivity (~8 mOhm-cm). We also ascertained that this amorphous oxide can be a promising magneto-electric coupling layer to  $\text{BiFeO}_3$  that can also be used as a contact electrode by demonstrating at least  $10^{10}$  ferroelectric switching cycles of  $\text{BiFeO}_3$ .

## Results and Discussion

The microstructure, compositional homogeneity and the chemical state of each of the metals in FDTO films were investigated by a combination of high-resolution imaging and electron energy loss spectroscopy (EELS) in the TEM and x-ray photoelectron spectroscopy (XPS). Figure 1(a) shows a representative FDTO film (deposited at room temperature under  $2 \times 10^{-6}$  Torr pressure) sandwiched between the underlying quartz substrate and a protective Au overlayer. Nano-diffraction patterns from the FDTO layer marked by the red box are shown in the bottom left panel in Fig. 1(a) and consist of a diffuse pattern that is typical of an amorphous microstructure. In contrast, the diffraction pattern from the blue box within the top Au layer showed sharp rings corresponding to a polycrystalline microstructure. Areal concentration distribution of Fe, Dy, Tb and O by EELS measured from the area marked by the purple rectangle showed that the distribution of the elements was homogeneous over the probed area, as shown in Fig. 1(b). Small regions showed higher concentrations of iron cations due to variations in the thickness of the cross-section sample causing the lanthanide peaks to be under-estimated at the expense of over-estimating the iron peak. No evidence of metal clustering or structural order was found from such TEM studies indicating that FDTO films were amorphous oxides. In order to obtain the film thicknesses and corresponding densities, the FDTO films were also characterized using X-Ray Reflectivity (XRR). There is a slight trend of the densities decreasing and thickness values increasing as oxygen deposition pressure increases for the films grown at same deposition conditions (see Fig. S1, supplementary information). Given that the deposition times were kept constant, the increase in the thickness was attributed to increasing volume with increasing oxygen pressures as a result of higher oxygen incorporation.

The oxidation state of the metal cations for films prepared under varying oxygen pressures was investigated using XPS measurements. In Fig. 1(c), the peaks obtained from iron 2p (top panel), terbium and dysprosium 4d (middle panel), and oxygen 1s (bottom panel) for the film deposited at  $2 \times 10^{-6}$  Torr are shown. The key result

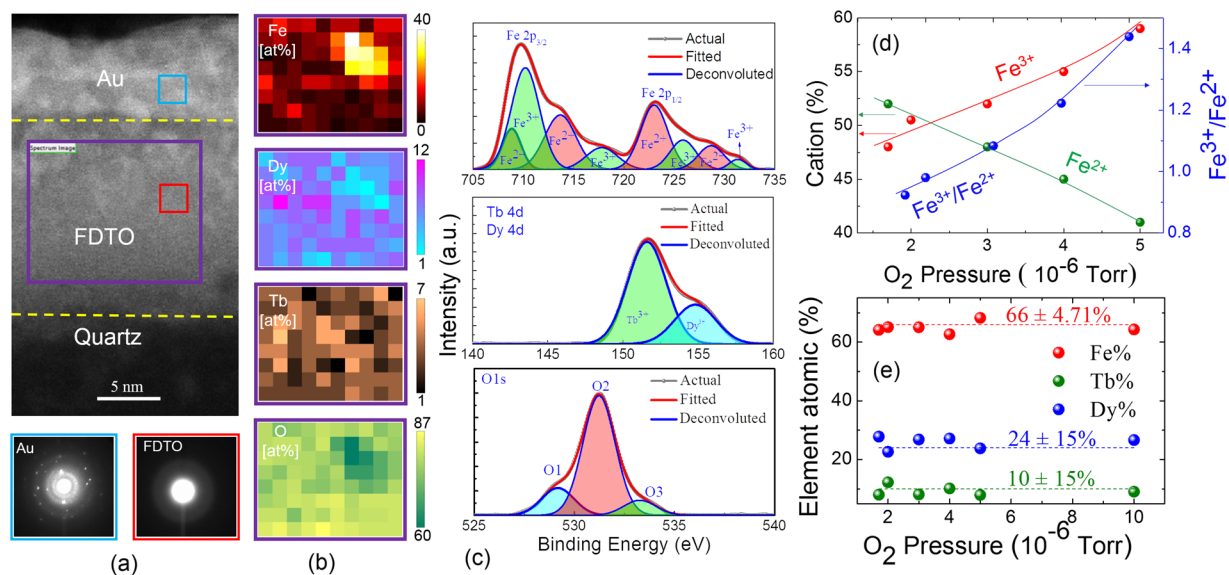


**Figure 1.** Amorphous microstructure and cation composition of FDTO. Panel (a) HRTEM image showing protective top Au layer, middle FDTO layer, and bottom quartz layer (top panel). Bottom panels show the diffraction pattern taken from the FDTO layer (red box) and Au layer (blue box). Panel (b) The elemental distribution of Fe, Dy, Tb and O (top to bottom) obtained from EELS spectrum of the area inside the purple box. (c) XPS signal and peak fitting for the various metals and oxygen. (d) Quantification of the observed valence states of Fe ( $\text{Fe}^{2+}$  and  $\text{Fe}^{3+}$ ; left y-axis), and the ratio of  $\text{Fe}^{3+}/\text{Fe}^{2+}$  (right y-axis) across varying oxygen pressure from  $1 \times 10^{-6}$  to  $5 \times 10^{-6}$  Torr. (e) Atomic % of the three metals measured by energy dispersive spectroscopy for films deposited at the various pressures, showing elemental composition of a-FDFO to be very close to that of the metallic target and consistent over all pressures. For Figure (a–c), a film deposited at  $2 \times 10^{-6}$  Torr of pressure was used.

was that no metallic peaks were seen from iron, terbium, and dysprosium for all the pressures investigated suggesting that the metal constituents were completely oxidized. The XPS spectra taken from all FDFO films deposited at varying oxygen pressures are shown in Fig. S2 (see supplementary information). For the entire pressure range investigated, terbium showed XPS peaks corresponding to the composition of  $\text{Tb}_4\text{O}_7$ , which is a mixed phase of  $\text{Tb}^{3+}$  and  $\text{Tb}^{4+}$  with excitation at  $151.6 \pm 0.2$  eV, while dysprosium showed excitation corresponding to  $\text{Dy}_2\text{O}_3$ , which occurs at  $154.7 \pm 0.1$  eV. On the other hand, the behavior of the iron cation states of  $\text{Fe}^{3+}$  to  $\text{Fe}^{2+}$  changed systematically with oxygen pressure. Using peak positions obtained from the standard XPS database, the  $\text{Fe}^{2+}$  and  $\text{Fe}^{3+}$  peaks could be decoupled thus allowing quantification of the two valence states of iron. Figure 1(d) shows the % $\text{Fe}^{2+}$  decreasing and % $\text{Fe}^{3+}$  increasing with increasing oxygen pressure. While the ratio  $\text{Fe}^{3+}/\text{Fe}^{2+}$  was observed to increase with increasing oxygen pressure, all the films were found to be richer in  $\text{Fe}^{2+}$  compared to in  $\text{Fe}_3\text{O}_4$ , where the ratio of  $\text{Fe}^{3+}/\text{Fe}^{2+}$  is 2. These results validated the conclusion that the thin films made by room-temperature deposition correspond to amorphous materials with completely oxidized metal constituents. The co-existence of  $\text{Fe}^{3+}/\text{Fe}^{2+}$  is one of the key aspects of using an amorphous layer such as FDFO, thus enabling conduction through hopping mechanisms as well as facilitating magnetism. The cationic stoichiometry of the oxide was verified by using energy dispersive X-ray spectroscopy in an SEM to measure the metallic compositions along with summing the oxygen content according to the stoichiometry of the metal oxides identified by XPS. Figure 1(e) shows that the atomic percentage of Fe, Tb, and Dy were found to be  $66 \pm 10\%$ ,  $10 \pm 15\%$  and  $24 \pm 15\%$  respectively in the FDFO films, which is consistent with the metal composition of the Terfenol-D target (Fe: 66%, Tb: 10%, and Dy: 24%), and hence indicating that the average chemical composition of grown films is  $\text{Fe}_{0.66}\text{Dy}_{0.24}\text{Tb}_{0.1}\text{O}_{7-x}$ .

The electronic band gap of the FDFO thin films were investigated by a combination of optical and XPS techniques. In Fig. 2(a) the Tauc plot derived from optical transmission spectroscopy measurements (see Fig. S3, supplementary information) revealed that the films had a direct bandgap ranging from 2.5 eV (oxygen pressure  $1 \times 10^{-6}$  Torr) to 3.2 eV (oxygen pressure  $1 \times 10^{-3}$  Torr). The indirect bandgap was also seen to increase from 1.7 eV to 2.8 eV as pressure increased across the same range. The optical transmission measurements, shown in Supplementary Fig. S3(a) indicated that the films were optically transparent, although transparency decreased with decreasing oxygen pressure. To further elucidate the band structure, XPS measurements were used to measure the work function and valence band maximum (VBM) of the FDFO films deposited at  $1 \times 10^{-6}$  Torr and  $5 \times 10^{-6}$  Torr. While both films had an identical work function of 4.4 eV (see Fig. S3(d),(e), supplementary information), the Fermi level was found to lie 0.25 eV inside the valence band for the lower pressure film ( $1 \times 10^{-6}$  Torr), while it was 0.34 eV above the valence band for the higher pressure film ( $5 \times 10^{-6}$  Torr). Considering all the aforementioned pieces of information, along with prior understanding of band structure of amorphous semiconductor films, the band structure of amorphous FDFO can be envisioned as shown in Fig. 2(b). The important information here is that the band-gap suggested a semiconducting material whose energy gap could be tuned

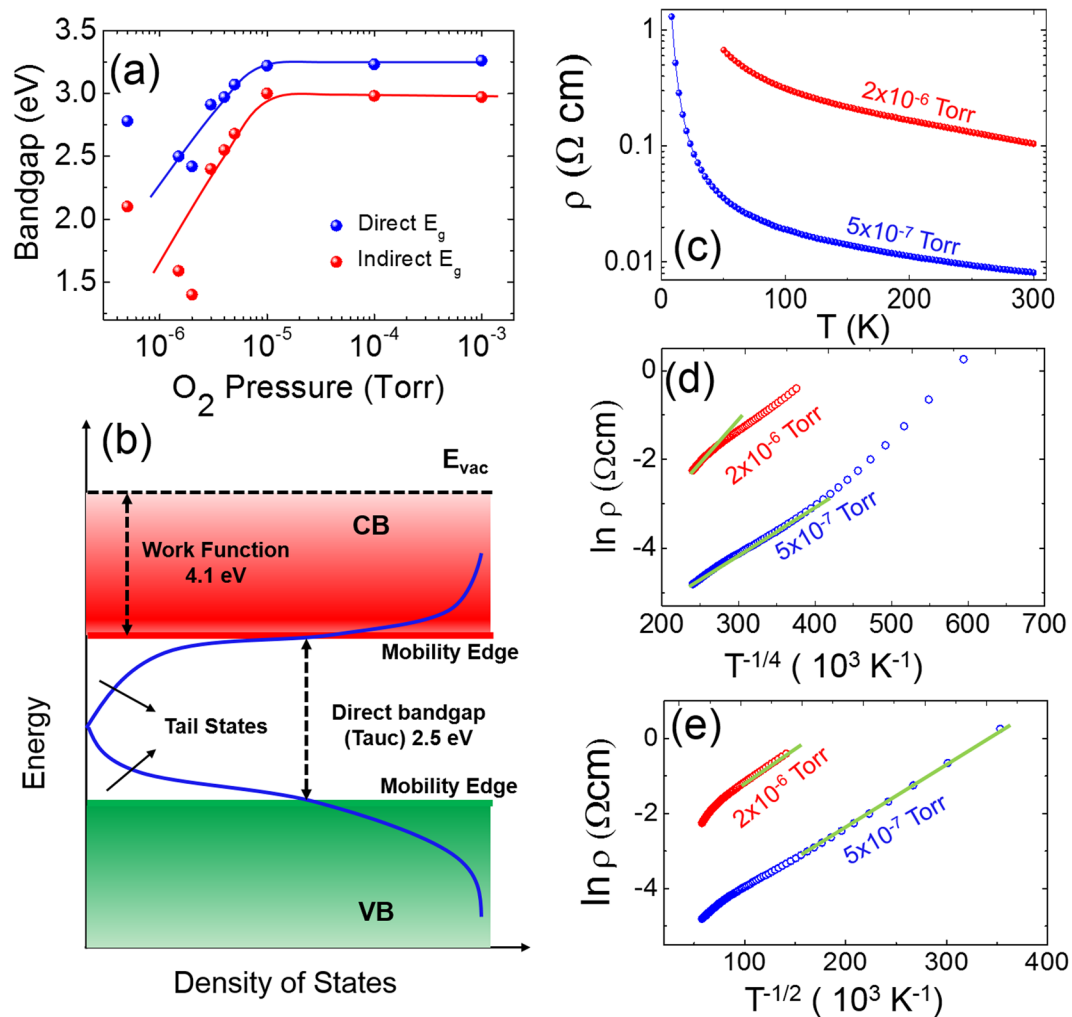


**Figure 2.** Band-gap and electrical conductivity of amorphous FDTO. (a) Direct and indirect bandgap obtained from Tauc plot for thin films of a-FDFO deposited at oxygen pressures ranging from  $5 \times 10^{-7}$  Torr to  $1 \times 10^{-3}$  Torr. (b) Schematic of band structure of a-FDFO film deposited at  $2 \times 10^{-6}$  Torr showing the bandgap, work function, and mobility edges and tail states at the conduction and valence bands. (c) Resistivity as a function of temperature from 3 K to 300 K for two a-FDFO films deposited at two different oxygen pressures. Both curves show semiconductor behavior. (d), (e) Fit of temperature dependent resistivity to (d) 3-D variable range hopping model, showing good fit for both a-FDFO films above 100 K, and (e) 1-D variable range hopping model showing good fit for both films below 100 K.

by changing the oxygen pressure during growth. In addition, the position of the valence band maximum with respect to the Fermi level indicated FDFO to be a p-type semiconductor. This band structure analysis suggests the interesting possibility that quantum-well homo-structures could be made in a monolithic film by simply tuning the oxygen pressure during growth.

The transport properties of the films were investigated as a function of temperature to determine the nature of electronic conduction. Figure 2(c) shows the temperature-dependent resistivity between 3–300 K for the lower oxygen pressure films. The films displayed decreasing resistivity with increasing temperature, indicative of semiconducting behavior. Films deposited at pressures of  $1 \times 10^{-5}$  Torr and higher show extremely high resistivity at room temperature (see Fig. S4(a), supplementary information), which did not change much with changing oxygen pressure, and thereby suggests that the films deposited at higher oxygen pressures are highly insulating in nature. The conduction in many disordered systems can be explained by either variable-range hopping (VRH) or small-polaron hopping (SPH)<sup>39,40</sup>. The magnitude of conductivity observed in the FDFO system for deposition pressures below  $5 \times 10^{-6}$  Torr, as shown in Fig. 2(c), is of the order of  $10^{-1}$  to  $10^{2-1}$  cm<sup>-1</sup> and is much higher than those typically observed for systems with SPH conduction (highest being  $10^{-3-1}$  cm<sup>-1</sup> for vanadium oxide<sup>41</sup>), VRH seemed the more likely conduction mechanism. In 3-D VRH, the DC conductivity, is related to the temperature through a parameter, which can be expressed as  $1/(d+1)$ ,  $d$  being the space dimension of the system [38, 39] and  $1/4 \ll 1.0$ . The value of  $d$  is largely determined by the localized DOS near the Fermi level, as explained by Singh and Shimakawa<sup>42</sup>. In case of a constant DOS,  $d = 1/2$  is obtained; however, the value of  $d$  can be less than unity in the case of modified VRH if the fractal nature of the system is taken into account<sup>39,43</sup>. Therefore, selecting

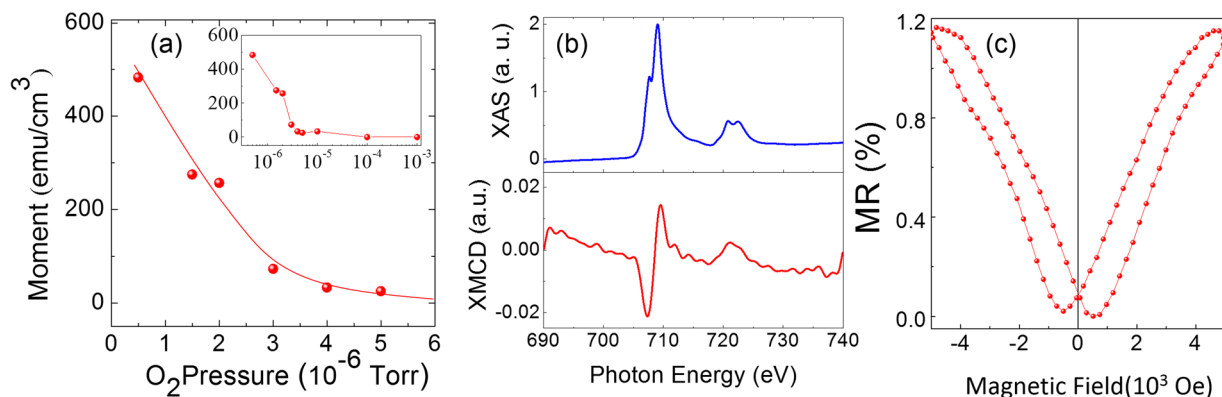


**Figure 3.** Magnetic properties of amorphous FDTO films. **(a)** Room temperature magnetic moment of FDTO films as a function of oxygen pressure during deposition. Inset shows the magnetic moment for a wider range of deposition pressure (up to  $10^{-3}$  Torr) with a logarithmic x-axis. **(b)** XAS (top) and XMCD (bottom) data from an FDTO film deposited at  $2 \times 10^{-6}$  Torr showing the magnetic signal aligning with the absorption energy from  $\text{Fe}^{3+}$  peak. **(c)** Room temperature magnetoresistance of FDTO film deposited at  $4 \times 10^{-6}$  Torr showing positive magnetoresistance.

the correct model to apply is not trivial. In the case of FDTO, the most typical fit of 3-D VRH was applied to the low-temperature resistance data for both the films. As Fig. 2(d) shows, the experimental data fit very well with 3-D VRH (with  $T^{-1/4}$ ) down to 100 K, below which a 1-D VRH ( $T^{-1/2}$ ) fit the experimental data best, as shown in Fig. 2(e). The transition from 3D-VRH to 1D-VRH is a result of Coulomb interactions playing a greater role at low temperature where the kinetic energy of the electrons is also low.

SQUID magnetometry of the FDTO films, deposited at varying oxygen pressure on quartz substrates, reveals a systematic variation of the saturation moment with the growth oxygen pressure, Fig. 3(a) (for details, see Fig. S4(b), supplementary information). For films deposited at oxygen pressures below  $3 \times 10^{-6}$  Torr the magnetic moment was  $>100$  emu/cc at room temperature. The inset shows that those films prepared at oxygen pressures above  $1 \times 10^{-5}$  Torr exhibited no room-temperature remanent magnetism. Based on the presence of iron cation states in these films, X-ray magnetic circular dichroism (XMCD) measurements (Fig. 3(b)) were made on FDTO films deposited at  $2 \times 10^{-6}$  Torr to confirm that one of the sources of magnetism was the iron cation state and not metallic iron. The split peak appearing in the X-ray absorption spectroscopy data in the top panel of Fig. 3(b) is evidence of  $\text{Fe}^{3+}$  in the film, consistent with Fig. 1(d). X-ray measurements at the iron  $L_{2,3}$  edges revealed strong dichroism [Fig. 3(b), bottom panel], indicative of a net ferromagnetic moment, arising from the iron site. This result further supports the ferromagnetic state of the film, consistent with the SQUID results.

These magnetic, optical, and transport properties demonstrate that FDTO is an amorphous semiconductor displaying magnetic ordering at room temperature. However, in order for it to be useful in spintronic devices, the spin and charge carriers in the system must be coupled. One way to prove this is by confirming magnetoresistance in the system. Figure 3(c) shows the room-temperature magnetoresistance curve of an FDTO film deposited at  $2 \times 10^{-6}$  Torr, demonstrating positive magnetoresistance where resistance increases with increasing magnetic field, a phenomenon that has been reported in several disordered and granular magnetic systems<sup>44–48</sup>. Although the %MR in FDTO is lower than that in  $\text{Fe}_3\text{O}_4$ , the existence of magnetoresistance confirmed the coupling between spin and charge carriers in FDTO, and hence consolidating its utility towards magnetoelectric devices.

In order to examine the applicability of FDTO thin films for magnetoelectric devices, we studied the coupling to a known multiferroic,  $\text{BiFeO}_3$  (BFO). Figure 4(a) shows a cross-section high-resolution TEM image of amorphous FDTO film grown on single-crystal BFO/ $\text{SrRuO}_3$  at  $2 \times 10^{-6}$  Torr of oxygen pressure. The interface between FDTO and BFO was sharp and without any contamination, and the epitaxial oxide layers of BFO and  $\text{SrRuO}_3$  did not show any detrimental effect after the growth of FDTO films (see Fig. S5(a), supplementary information) The magnetic behavior of this system was compared to FDTO grown on quartz and is shown in Fig. 4(b). A substantial increase in coercivity for in-plane configuration, from  $\sim 10$  to  $\sim 300$  Oe, was seen for the FDTO on BFO compared to that on quartz. This strongly points to exchange coupling between the layers suggesting that the magnetic order in FDTO can couple to the underlying canted magnetic moments of BFO. Such a large enhancement in coercivity (observed in several samples, see Fig. S5(b), supplementary information) can be understood by the fact that the in-plane coercivity for a ferromagnetic metallic film (CoFe) changes, due to exchange coupling with BFO, from  $\sim 10$  Oe to  $\sim 100$  Oe<sup>32,36</sup>.

With this understanding of the magnetic coupling between the FDTO and BFO, the next step was to study the possibility of magnetoelectric coupling, i.e., electric field manipulation of the magnetic state of the FDTO. In order to do this, we have typically been using a spin valve as a sensing element<sup>8,32</sup>. Thus, as a first step, we fabricated a standard CoFe-Cu-CoFe giant magnetoresistance (GMR) heterostructure on the FDTO. Figure 4(c) shows the corresponding device schematic, where a bottom  $\text{Co}_{0.9}\text{Fe}_{0.1}$  layer coupled to the BFO layer through the ferromagnetic FDTO, resulting in its higher coercivity compared to the top  $\text{Co}_{0.9}\text{Fe}_{0.1}$  layer. This difference in coercivity between the top and the bottom  $\text{Co}_{0.9}\text{Fe}_{0.1}$  layers gives rise to the GMR signal. Figure 4(d) shows a peak 0.35% GMR signal of the heterostructure when no voltage was applied across the BFO. Application of +7 V left

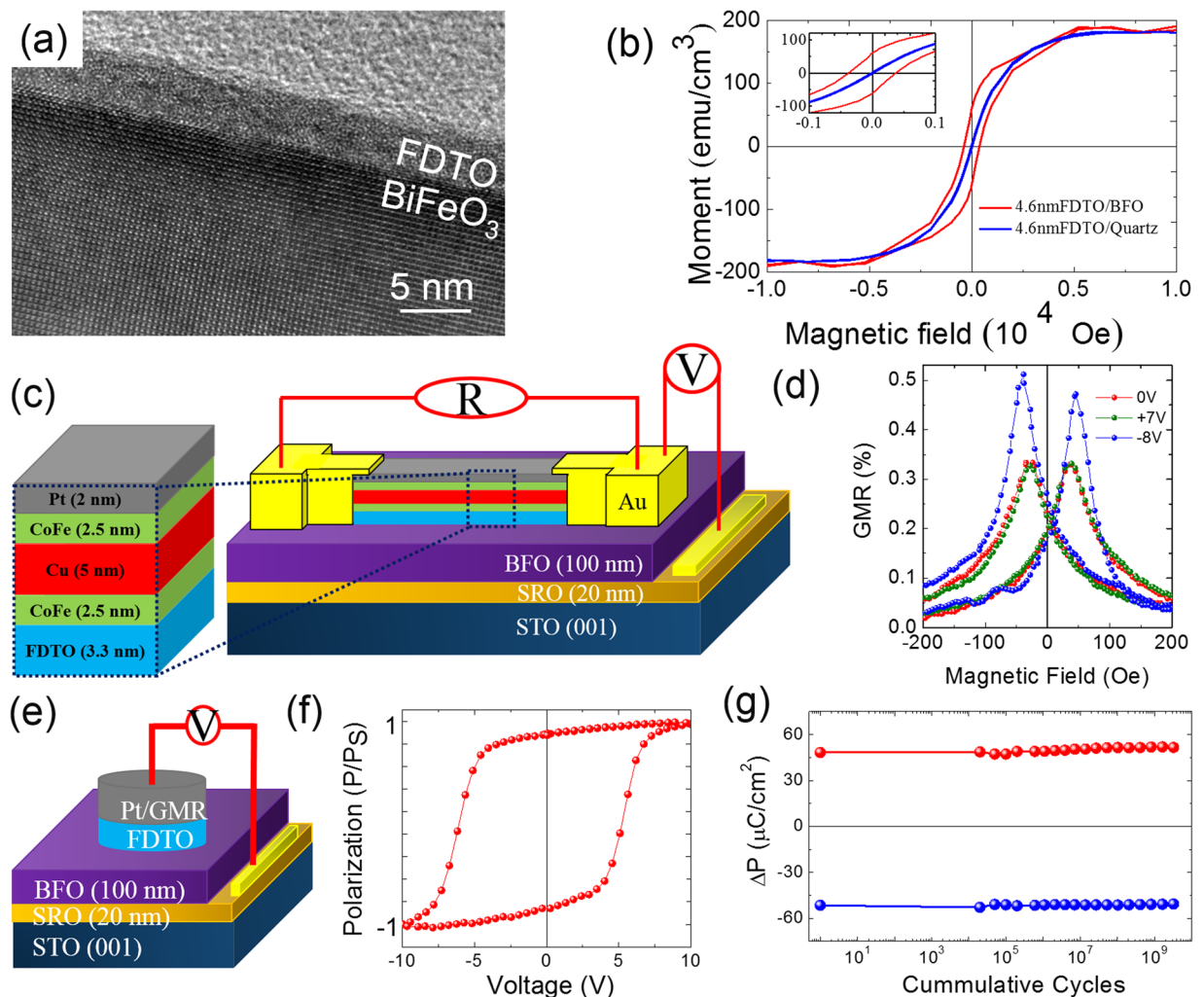


**Figure 4.** Magnetoelectric spintronics with ferromagnetic amorphous FDTO thin films. **(a)** HRTEM image of the interface between amorphous FDTO deposited at  $2 \times 10^{-6}$  Torr at room temperature on crystalline BFO. **(b)** Magnetic moment (emu/cm<sup>3</sup>) loops taken at room temperature, showing enhanced coercivity of the FDTO/BFO film (red) as compared to the FDTO/quartz (blue), demonstrating magnetic coupling between FDTO and BFO thin film at room temperature. **(c)** Schematic of GMR heterostructure used to study ME switching capabilities of amorphous FDTO. **(d)** GMR signal as a function of applied magnetic field at room temperature showing change in the GMR signal upon switching BFO ferroelectric polarization from one state to another with the application of +7 V (green) to -8 V (blue). **(e)** Schematic of a-FDTO/BFO capacitor used to test the robustness of FDTO layer as a top electrode for BFO. **(f)** Ferroelectric hysteresis loop of the capacitor in **(e)** at room temperature showing nearly rectangular closed hysteresis. **(g)** Fatigue test of the capacitor in **(e)** showing stable polarization for  $\sim 10^{10}$  cumulative switching cycles.

the GMR signal unchanged, but application of -8 V markedly changed the GMR signal of the heterostructure. We have seen such a resistance modulation in several devices (see Fig. S5(c), supplementary information). The ferroelectric switching of BFO thin films with the amorphous FDTO as a top contact electrode was also tested and hysteresis loops were measured at room temperature on the capacitor device schematically shown in Fig. 4(e). The device showed stable polarization-electric field hysteresis loops as can be seen in Fig. 4(f), where the ferroelectric switching voltages match well with the magnetoelectric switching fields of spin valve devices fabricated on FDTO/BFO/SRO heterostructure (see Fig. 4d). In addition, bipolar polarization fatigue measurements showed at least  $\sim 10^{10}$  switching cycles, as seen in Fig. 4(g), a performance that is better than that for commonly used metallic electrodes such as platinum and comparable to the best crystalline oxide electrodes for BiFeO<sub>3</sub><sup>33–35</sup>.

In conclusion, we have shown a new thin film oxide magnetic material (Fe<sub>0.66</sub>Dy<sub>0.24</sub>Tb<sub>0.1</sub>)<sub>3</sub>O<sub>7-x</sub>, that exhibits a desirable combination of magnetic moment ( $\sim 200$  emu/cc) and low enough resistivity ( $\sim 8$  mOhm-cm). The magnetism in the FDTO couples to the BiFeO<sub>3</sub> at room temperature resulting in magnetoelectric switching that was probed through the fabrication of a simple spin valve structure. Also, FDTO could be used as a contact electrode and demonstrated stability with no indication of fatigue even after  $\sim 10^{10}$  ferroelectric switching cycles of BiFeO<sub>3</sub>. This work points to several directions for further research. An in-depth study of the degradation mechanisms would be extremely valuable. There has been very little use of amorphous metals as contacts to ferroelectrics and

this work may be useful in that regard. Similarly, it would be of interest to create tunnel junctions using the FDTO as the magnetic layer (instead of the CoFe-Cu-CoFe on the FDTO), thus probing the spin transport directly.

## Methods

**Synthesis and fabrication.** Thin films (20–30 nm) of FDTO were deposited from a commercially available metal alloy target, Terfenol-D (66% Fe, 24% Dy, 10% Tb) by pulsed laser deposition using a KrF excimer laser was used with wavelength of 248 nm, rep rate of 10 Hz, and energy density of 1 J/cm<sup>2</sup>. Quartz substrates were used to allow for transport, magnetic, and optical measurements on the films, as well as for GIXRD, XRR, TEM, and XPS. FDTO films were deposited at room temperature and in dynamic oxygen pressure environments of  $5 \times 10^{-7}$  Torr to  $1 \times 10^{-3}$  Torr. For the device studies, FDTO was grown as described above at  $3 \times 10^{-6}$  Torr on BFO (100 nm)/SRO (20 nm)/SRO (001) substrates in the presence of a magnetic field (~2500 Oe). The BFO and SRO were grown using the methods described in ref.<sup>32</sup> GMR structures of Co<sub>0.9</sub>Fe<sub>0.1</sub> (2.5 nm)/Cu(5 nm)/Co<sub>0.9</sub>Fe<sub>0.1</sub> (2.5 nm) were deposited on FDTO(4 nm)/BFO(100 nm)/SRO(20 nm)/STO using magnetron sputtering techniques and subsequently the micron sized spin valves were created by conventional photolithography techniques. These same structures were used for ferroelectric measurements. The lateral dimension of the device was about 50 μm, while the device width was about 10 μm. Contacts were made by careful wire bonding to the Pt contact pads.

**Characterization techniques.** *Microstructure and chemical composition.*

- **X-ray reflectivity (XRR) and X-ray diffraction (XRD):** XRR was performed on the films Panalytical X'Pert<sup>3</sup> MRD X-ray diffractometer in order to measure the thickness and density of the FDTO films. A slit of 1/16 was used on the beam side to optimize reflectivity signals. Fitting of the XRR fringes were done using the reflectivity software that came with the instrument. The same instrument was used to measure X-ray diffraction peaks of the BFO films.
- **Transmission electron microscopy (TEM):** The microstructure of the as-deposited and annealed FDTO films were further investigated in TEM to look for the presence/absence of any nanoclusters and the interfacial conditions. High-resolution TEM images, EELS spectra, and nano-diffraction patterns were taken in Ultra-STEM 200 microscope at the Center for Nanophase Materials Science at Oak Ridge National Lab, FEI Titan X 300KV microscope and F20 UT Tecnai 200KV at Lawrence Berkeley National Lab.
- **X-ray photoelectron spectroscopy (XPS):** The as-prepared and annealed FDTO films were characterized by XPS to look at the cation states near the surface of the film. XPS measurements were done at room temperature in an ion-pumped chamber (evacuated to  $2 \times 10^{-9}$  Torr) of an PE-PHI5400 spectrometer, employing Al-Kα radiation (BE = 1486.6 eV) of about 4 mm spot size. The binding energy (BE) for the samples was calibrated by setting the measured BE of C 1s to 284.6 eV. Peakfit software was further used to identify the chemical state of multifaceted Fe 2p, Dy Tb 4d and O 1s spectra according to the previous reports. XPS measurements were also done to measure the work function of the as-prepared films. The system used for this purpose was a Kratos AXIS Ultra system which has a monochromatic Al K-alpha source, with a hemispherical analyzer. A charge correction to C 1s peak was applied during data fitting.

**Optical properties.** The optical characterization techniques utilized here were similar to those in our previous work<sup>37</sup>. Ultra-violet-Visible (UV-Vis) transmission spectra were obtained for all thin films deposited on quartz using an Ocean Optics spectrometer with a He-Ne light source that allowed measurements to be made between 300 nm to 900 nm, with integration time of 1 ms and 100 scans to average. Transmission spectra were acquired at five different locations of each sample to ensure homogeneity of the film thickness. Tauc plots for were generated by first converting the transmission values (% T) to absorbance using Beer-Lambert's law and then dividing by the film thickness to get the absorption coefficient as a function of the probing wavelength. The Tauc plot was made with y-axis as  $(\alpha h\nu)^{1/m}$  as a function of  $h\nu$  (the wavelength in energy units). A tangent was drawn at the region of the plot with sharp increase, which was then extrapolated to cut the x-axis at the band-gap value;  $m = 1/2$  was used to obtain a direct band gap value and  $m = 2$  was used to obtain indirect bandgap value assuming bands are parabolic.

**Transport properties.** Four-probe sheet resistance of the samples were measured at room temperature in the Van der Pauw geometry using Ecopia HMS 3000 Hall measurement system. Pt contact pads were deposited on the four corners of the samples prior to measurement. The samples were mounted on an SPCB-1 spring clipboard that comes with the HMS system. The contact probes were gold coated and spring loaded. Temperature and field dependent resistivity measurements were made using a Quantum Design Physical Property System. High purity silver epoxy from SPI Supplies and gold wires of 25 μm diameter were used as contact electrodes and wiring respectively. Measurements were made using the Van der Pauw configuration as described above to eliminate contact resistance at the sample-electrode interface, at intervals of 5 K.

**Magnetic properties.** Superconducting quantum interference device (SQUID) was used mainly to measure magnetic moment as a function of magnetic field. The system used was a Quantum Design Magnetic Property Measurement System using brass as a sample holder at UTK, and plastic drinking straw as sample holder at UCB. Magnetic fields of up to 5 Tesla were supplied for these measurements. Samples on quartz typically contributed to a diamagnetic background signal, which was subtracted to get the saturation magnetization for the FDTO films. Magnetic moment as a function of temperature were also measured for the as-prepared films having different R values using a vibrating sample magnetometer by our collaborator at North Carolina A&T State University. All samples for magnetic measurement were handled using non-magnetic, teflon tip tweezers to prevent contamination from magnetic impurities.

*X-ray magnetic circular dichroism (XMCD).* XMCD measurements were carried out at beamline 6.3.1 of the Advanced Light Source, Lawrence Berkeley National Laboratory, focused on the Fe L-edge. The measurements used fixed circularly polarized X-rays at 300 K, in total electron yield configuration with grazing angle of 30°. To ensure that the XMCD signal was of magnetic origin, the measurements were repeated with opposite polarization and it was confirmed that the asymmetry reversed.

*Magnetoresistance (MR).*

- **Normal MR:** MR was measured using a home-built measurement system. The system used an electro-magnet that was capable of going up to 6000 Oe, a Keithley 6221 for supplying AC current, and a Stanford SR865A lock-in amplifier to measure the voltage. A LabVIEW program was developed to interface with all the instruments, and collect, plot and save data. The contacts were made by wirebonding Ag contact pads on the samples to contact pads on a chip holder that was used to mount the sample at the center of the magnetic field. The magnetic field was supplied IP to the plane of the sample for this measurement.
- **Giant MR (GMR):** GMR signal of the devices were measured using the same home-built system as described in the normal MR section. Magnetic field was supplied IP with respect to the plane of the sample. In addition, an Agilent signal generator was used to customize pulse voltages to be supplied as bias across the BFO thin film. A Keithley 6517a was also used for this purpose to supply a constant DC voltage when needed.

Received: 6 August 2019; Accepted: 6 January 2020;

Published online: 27 February 2020

## References

1. Awschalom, D. D. & Flatté, M. E. Challenges for semiconductor spintronics. *Nat. Phys.* **3**, 153 (2007).
2. Manipatruni, S., Nikonov, D. E. & Young, I. A. Beyond CMOS computing with spin and polarization. *Nat. Phys.* **14**, 338 (2018).
3. Liang, K. *et al.* Multiferroic magnetoelectric coupling effect of bilayer  $\text{La}_{1.2}\text{Sr}_{1.8}\text{Mn}_2\text{O}_7/\text{PbZr}_{0.3}\text{Ti}_{0.7}\text{O}_3$  complex thin film. *Phys. Lett. A* **381**, 1504 (2017).
4. Liu, M. *et al.* Giant Electric Field Tuning of Magnetic Properties in Multiferroic Ferrite/Ferroelectric Heterostructures. *Adv. Func. Mat.* **19**, 1826 (2009).
5. Riestler, S. *et al.* Toward a low-voltage multiferroic transistor: Magnetic (Ga,Mn)As under ferroelectric control. *APL* **94**, 063504 (2009).
6. Wu, S. M. *et al.* Reversible electric control of exchange bias in a multiferroic field-effect device. *Nat. Mat.* **9**, 756 (2010).
7. Palneedi, H., Annareddy, V., Priya, S. & Ryu, J. Status and perspectives of multiferroic magnetoelectric composite materials and applications. *Actuators* **5**, 9 (2016).
8. Manipatruni, S. *et al.* Scalable energy-efficient magnetoelectric spin-orbit logic. *Nature* **565**, 35 (2019).
9. Adurodija, F., Izumi, H., Ishihara, T., Yoshioka, H. & Motoyama, M. The electro-optical properties of amorphous indium tin oxide films prepared at room temperature by pulsed laser deposition. *Sol. En. Mat. Sol. Cells* **71**, 1 (2002).
10. Chen, Y.-C. *et al.* High-stability oxygen sensor based on amorphous zinc tin oxide thin film transistor. *APL* **100**, 262908 (2012).
11. Chiku, M., Takeda, H., Matsumura, S., Higuchi, E. & Inoue, H. Amorphous Vanadium Oxide/Carbon Composite Positive Electrode for Rechargeable Aluminum Battery. *ACS Appl. Mat. Int.* **7**, 24385 (2015).
12. Chiang, H. Q., Wager, J. F., Hoffman, R. L., Jeong, J. & Keszler, D. A. High mobility transparent thin-film transistors with amorphous zinc tin oxide channel layer. *APL* **86**, 013503 (2005).
13. Hosono, H. Ionic amorphous oxide semiconductors: Material design, carrier transport, and device application. *J. Non-Cryst. Sol.* **352**, 851 (2006).
14. Hosono, H., Kim, J., Toda, Y., Kamiya, T. & Watanabe, S. Transparent amorphous oxide semiconductors for organic electronics: Application to inverted OLEDs. *PNAS* **114**, 233 (2017).
15. Huang, J.-S. Amorphous zinc-doped silicon oxide (SZO) resistive switching memory: manipulated bias control from selector to memristor. *et al. J. Mater. Chem. C* **2**, 4401 (2014).
16. Idota, Y., Kubota, T., Matsufoji, A., Maekawa, Y. & Miyasaka, T. Tin-Based Amorphous Oxide: A High-Capacity Lithium-Ion-Storage Material. *Science* **276**, 5317 (1997).
17. Kamiya, T. & Hosono, H. Material characteristics and applications of transparent amorphous oxide semiconductors. *NPG Asia Mater* **2**, 15 (2010).
18. Kim, M.-G. *et al.* High-Performance Solution-Processed Amorphous Zinc-Indium-Tin Oxide Thin-Film Transistors. *JACS* **132**, 10352 (2010).
19. Li, X., Zhang, L., Dong, H., Xia, T. & Huang, Z. Bismuth oxide coated amorphous manganese dioxide for electrochemical capacitors. *Sol. St. Sci.* **43**, 46 (2015).
20. Litvinov, J. *et al.* Development of pinhole-free amorphous aluminum oxide protective layers for biomedical device applications. *Surf. Coat. Tech.* **224**, 101 (2013).
21. Hosono, H., Kikuchi, N., Ueda, N. & Kawazoe, H. Working hypothesis to explore novel wide band gap electrically conducting amorphous oxides and examples. *J. Non-Cryst. Solids* **198-200**, 165 (1996).
22. Yabuta, H. *et al.* High-mobility thin-film transistor with amorphous  $\text{InGaZnO}_4$  channel fabricated by room temperature rf-magnetron sputtering. *APL* **89**, 112123 (2006).
23. Kamiya, T., Nomura, K. & Hosono, H. Present status of amorphous In-Ga-Zn-O thin-film transistors. *Sci. Tech. Adv. Mat.* **11**, 044305 (2010).
24. Dietl, T. A ten-year perspective on dilute magnetic semiconductors and oxides. *Nat. Mater.* **9**, 965 (2010).
25. Coey, J. Dilute magnetic oxides. *Current Opinion in Sol. St. Mat. Sci.* **10**, 83 (2006).
26. Matsumoto, Y. *et al.* Room-Temperature Ferromagnetism in Transparent Transition Metal-Doped Titanium Dioxide. *Science* **291**, 854 (2001).
27. Pearton, S. J., Heo, W. H., Ivill, M., Norton, D. P. & Steiner, T. Dilute magnetic semiconductor oxides. *Semic. Sci. Tech.* **19**, R59 (2004).
28. Sánchez, D., García-Hernández, M., Auth, N. & Jakob, G. Structural, magnetic, and transport properties of high-quality epitaxial  $\text{Sr}_2\text{FeMoO}_6$  thin films prepared by pulsed laser deposition. *JAP* **96**, 2736 (2004).
29. Ning, Z. *et al.* Magnetoelectric Coupling in Bilayers of  $\text{Pb}(\text{Zr}, \text{Ti})\text{O}_3$  Epoxy and Hot Pressed Manganite Perovskite. *Chin. Phys. Lett.* **23**, 463 (2006).
30. Li, X. W., Gupta, A., Xiao, G. & Gong, G. Q. Transport and magnetic properties of epitaxial and polycrystalline magnetite thin films. *JAP* **83**, 7049 (1998).

31. Wei, J. D. *et al.* Influence of the antiphase domain distribution on the magnetic structure of magnetite thin films. *APL* **89**, 122517 (2006).
32. Heron, J. T. *et al.* Deterministic switching of ferromagnetism at room temperature using an electric field. *Nature* **516**, 370 (2014).
33. Baek, S. *et al.* The Nature of Polarization Fatigue in BiFeO<sub>3</sub>. *Adv. Mat.* **23**, 1621 (2011).
34. Zhou, Y. *et al.* Mechanism of polarization fatigue in BiFeO<sub>3</sub>: The role of Schottky barrier. *APL* **104**, 012903 (2014).
35. Baek, S. H. & Eom, C. B. Reliable polarization switching of BiFeO<sub>3</sub>. *Phil. Trans. Royal Soc. London A: Math. Phys. Eng. Sci.* **370**, 4872 (2012).
36. Heron, J. T., Schlom, D. G. & Ramesh, R. Electric field control of magnetism using BiFeO<sub>3</sub>-based heterostructures. *App. Phys. Rev.* **1**, 021303 (2014).
37. Malasi, A. *et al.* Novel Iron-based ternary amorphous oxide semiconductor with very high transparency, electronic conductivity and mobility. *Sci. Rep.* **5**, 18157 (2015).
38. Taz, H. Transparent ferromagnetic and semiconducting behavior in Fe-Dy-Tb based amorphous oxide films. *et al. Sci. Rep.* **6**, 27869 (2016).
39. Shklovskii, B. I. & Efros, A. L. Electronic Properties of Doped Semiconductors. *Springer Series in Solid-State Sciences*, 45 (1984).
40. Kishimoto, N. & Morigaki, K. Optical Absorption and Infrared Photoconductivity in Amorphous Si–Au System. *Journal of the Physical Society of Japan* **46**, 497 (1979).
41. Adler, D., Fritzsche, H. & Ovshinsky, S. R., eds., Fundamental Problems Relating to the Electronic Structure of Amorphous Semiconductors. *Physics of Disordered Materials. Institute for Amorphous Studies Series*, 1985.
42. Singh, J. & Shimakawa, K. Electronic processes in amorphous semiconductors. *Advances in Condensed Matter Science*, CRC Press (2003).
43. van der Putten, D., Moonen, J. T., Brom, H. B., Brokken-Zijp, J. C. & Michels, M. A. Evidence for superlocalization on a fractal network in conductive carbon-black–polymer composites. *Physical review letters* **69**, 494 (1992).
44. Dho, J., Kim, B.-G. & Ki, S. Distinctive uniaxial magnetic anisotropy and positive magnetoresistance in (110)-oriented Fe<sub>3</sub>O<sub>4</sub> films. *JAP* **117**, 163904 (2015).
45. Wang, J. *et al.* Magnetoresistance sign change in iron-doped amorphous carbon films at low temperatures. *J. Phys. D: App. Phys.* **47**, 215002 (2014).
46. Lee, Y. J., Kim, Y. S. & Shin, H. K. Magnetoresistance of amorphous indium oxide films at the region of weak-strong localization crossover. *J. Phys. Cond. Mat.* **14**, 483 (2002).
47. Zeng, Y. *et al.* Large positive room temperature magnetoresistance in nanogranular FeCo–Si–N thin films. *Mat. Lett.* **110**, 27 (2013).
48. Movaghar, B. *et al.* A model for the anomalous magnetoresistance in amorphous semiconductors. *J. Phys. C: Sol. St. Phys.* **11**, 125 (1977).

## Acknowledgements

This work at UC Berkeley (R.R.) was funded by the NSF-SRC center, CAPSL and by an ARO grant (R.K and H.T.) W911NF-13-1-0428. H. T. acknowledges James Bullock for helping with XPS characterization, which was performed at the Joint Center for Artificial Photosynthesis, supported through the Office of Science of the U.S. Department of Energy under Award Number DESC0004993. Work at UC Berkeley and Lawrence Berkeley National Lab (A.J.) was supported by the Electronic Materials Program, funded by the Director, Office of Science, Office of Basic Energy Sciences, Material Sciences and Engineering Division of the U.S. Department of Energy under Contract No. DE-AC02-05CH11231. Z.C. acknowledges support from the U.S. Department of Energy, Office of Science, Office of Basic Energy Sciences, Materials Sciences and Engineering Division under Contract No. DE-AC02-05-CH11231 (Materials Project program KC23MP) for the development and study of novel functional materials. R.X. acknowledges support from the National Science Foundation under Grant DMR-1708615. L.W.M. acknowledges support from the Army Research Office under Grant W911NF-14-1-0104. H. T. acknowledges Dr. David Geohagan at CNMS for use of their STEM instrument.

## Author contributions

B.P., H.T., R.K. and R.R. designed the experiments. H.T. synthesized and characterized the FDTO films. B.P. fabricated the GMR devices and performed magnetic and ferroelectric measurements. Y.-L.H. has deposited BFO/SRO films. Z.C. has performed in XAS and XMCD measurements. V.T. and R.X. have done ferroelectric measurements. R.M., T.S.S., M.H., S.S. and A.J. performed XPS measurements. S.-L.H., C.L. and G.D. performed TEM/EELS imaging. H.T., B.P., L.W.M., R.K. and R.R. all made contribution to writing the manuscript. All authors discussed results and commented on the manuscript.

## Competing interests

The authors declare no competing interests.

## Additional information

**Supplementary information** is available for this paper at <https://doi.org/10.1038/s41598-020-58592-5>.

**Correspondence** and requests for materials should be addressed to B.P., R.R. or R.K.

**Reprints and permissions information** is available at [www.nature.com/reprints](http://www.nature.com/reprints).

**Publisher's note** Springer Nature remains neutral with regard to jurisdictional claims in published maps and institutional affiliations.



**Open Access** This article is licensed under a Creative Commons Attribution 4.0 International License, which permits use, sharing, adaptation, distribution and reproduction in any medium or format, as long as you give appropriate credit to the original author(s) and the source, provide a link to the Creative Commons license, and indicate if changes were made. The images or other third party material in this article are included in the article's Creative Commons license, unless indicated otherwise in a credit line to the material. If material is not included in the article's Creative Commons license and your intended use is not permitted by statutory regulation or exceeds the permitted use, you will need to obtain permission directly from the copyright holder. To view a copy of this license, visit <http://creativecommons.org/licenses/by/4.0/>.

© The Author(s) 2020